

Systematic investigation of the signal properties of polycrystalline HgI₂ detectors under mammographic, radiographic, fluoroscopic and radiotherapy irradiation conditions

Zhong Su, Larry E Antonuk, Youcef El-Mohri, Larry Hu, Hong Du, Amit Sawant, Yixin Li, Yi Wang, Jin Yamamoto and Qihua Zhao

Department of Radiation Oncology, University of Michigan, 519 W. William St., Argus Building 1, Ann Arbor, MI 48103-4943, USA

E-mail: antonuk@umich.edu

Received 28 January 2005, in final form 7 April 2005

Published 1 June 2005

Online at stacks.iop.org/PMB/50/2907

Abstract

The signal properties of polycrystalline mercuric iodide (HgI₂) film detectors, under irradiation conditions relevant to mammographic, radiographic, fluoroscopic and radiotherapy x-ray imaging, are reported. Each film detector consists of an ~ 230 to ~ 460 μm thick layer of HgI₂ (fabricated through physical vapour deposition or a screen-print process) and a thin barrier layer, sandwiched between a pair of opposing electrode plates. The high atomic number, high density and low effective ionization energy, W_{EFF} , of HgI₂ make it an attractive candidate for significantly improving the performance of active matrix, flat-panel imagers (AMFPIs) for several x-ray imaging applications. The temporal behaviour of current from the film detectors in the presence and in the absence of radiation was used to examine dark current levels, the lag and reciprocity of the signal response, x-ray sensitivity and W_{EFF} . The results are discussed in the context of present AMFPI performance. This study provides performance data for a wide range of potential medical x-ray imaging applications from a single set of detectors and represents the first investigation of the signal properties of polycrystalline mercuric iodide for the radiotherapy application.

1. Introduction

The replacement of analog x-ray imaging detectors (such as film-screen and x-ray image intensifier systems) by digital technologies has long been of widespread interest to the medical community (Capp 1981). In recent years, this transition has been accelerated through

the introduction of clinically-practical devices based on large area, active matrix, flat-panel imagers (AMFPIs) (Antonuk 2002, 2004, Street 2000). These devices consist of an x-ray detector material placed in contact with an underlying matrix of addressable pixels, each of which consists of a thin film transistor (TFT) coupled to a storage capacitor. AMFPIs may be divided into two types, indirect and direct, based on the method of detecting the incident radiation. In indirect detection AMFPIs, incident x-ray photons interact with a scintillating screen, typically $\text{Gd}_2\text{O}_2\text{S:Tb}$ or CsI:Tl , generating optical photons, some of which are detected by photodiodes built into the pixels. In direct detection AMFPIs, a layer of photoconductive material, typically 200–1000 μm of a-Se, converts x-rays into electron–hole pairs that drift under the influence of an externally applied electric field. The motion of these free charge carriers induces imaging signal in the pixels. The numerous advantages of AMFPIs (real-time readout, compact profile, superior image quality, etc) have led to their widespread acceptance in an increasing number of medical applications, including radiography, fluoroscopy, cardiac imaging, mammography and radiotherapy imaging (Antonuk 2002, Granfors *et al* 2001, Colbeth *et al* 2001, Ikeda *et al* 2003, Samei and Flynn 2003, Vedantham *et al* 2000, Zhao and Zhao 2003, Tousignant *et al* 2003).

While AMFPIs can provide high performance for most applications across the spectrum of medical x-ray imaging, a relatively low signal per interacting x-ray limits their performance under certain imaging conditions such as in fluoroscopic imaging at low exposures, and in mammographic imaging at high spatial frequencies. Under such conditions, the low number of optical photons or electron–hole pairs detected per interacting x-ray results in imaging signal levels that are modest relative to the electronic noise of the system (Antonuk *et al* 2000, El-Mohri *et al* 2003). In addition, for radiotherapy imaging, AMFPIs provide image quality superior to that of other technologies, but only about 1%–2% of the incident x-rays are detected (Antonuk 2002, Kruse *et al* 2002).

Several approaches are under investigation to improve AMFPI system performance in fluoroscopy and mammography through the enhancement of x-ray sensitivity (Antonuk *et al* 2000, El-Mohri *et al* 2003, Zhao *et al* 2004), which, for the purposes of this paper, is defined as the x-ray-generated signal measured per unit radiation exposure. A variety of strategies are also being examined to improve the x-ray detection efficiency with AMFPIs and other area detectors for radiotherapy imaging (Wowk *et al* 1993, Mosleh-Shirazi *et al* 1998, Sawant *et al* 2002, 2005, Seppi *et al* 2003, Pang and Rowlands 2004). A particularly attractive candidate detector material for addressing all of these needs is polycrystalline mercuric iodide (HgI_2). The properties of the single-crystal form of HgI_2 (Zuck *et al* 2003) lead to x-ray sensitivities on the order of ten times that of a-Se and on the order of five times that of $\text{Gd}_2\text{O}_2\text{S:Tb}$ and needle-structure forms of CsI:Tl . Since the fabrication of single-crystal HgI_2 in a form suitable for use with large area AMFPIs is not practical, polycrystalline forms of the material, which can be made in large areas using a variety of fabrication techniques, have been under investigation (Iwanczyk *et al* 2001, Street *et al* 2002, Zentai *et al* 2004, Antonuk *et al* 2004, Kang *et al* 2005). Moreover, the various methods for fabricating polycrystalline HgI_2 allow for the possibility of detector thicknesses well in excess of 1000 μm . Thus, given the high density and atomic number of HgI_2 , it is conceivable that relatively high detection efficiencies can be achieved for radiotherapy applications—for example, ~ 1000 – 3000 μm of detector material would yield efficiencies of $\sim 6\%$ – 14% at a beam energy of 6 MV.

As part of a programme to evaluate the feasibility of using polycrystalline HgI_2 for mammography, fluoroscopy and radiotherapy imaging, we have evaluated a number of simple film-sample detectors. Each of the detectors consists of a film of HgI_2 sandwiched between opposing planes of electrodes. The present evaluations are being performed in parallel with studies of direct detection AMFPI arrays coated with polycrystalline HgI_2 films

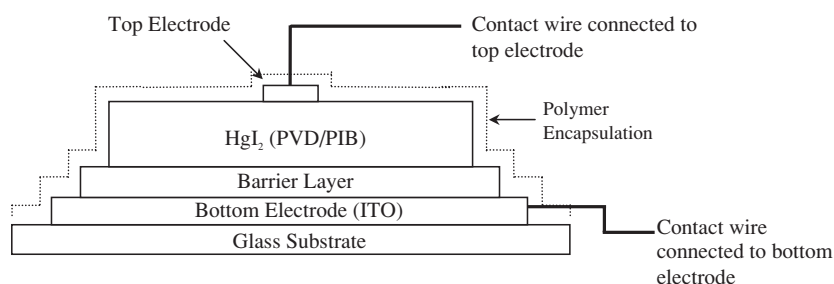


Figure 1. Schematic diagram (not to scale) illustrating a cross-sectional view of a HgI₂ film detector. Each glass substrate had an area of $\sim 25 \times 76 \text{ mm}^2$ and most of the surface was coated with ITO. In addition, the area of the HgI₂ material ranged from ~ 1290 to 1450 mm^2 . See the text for further details.

(Antonuk *et al* 2004). The goal of the research reported in this paper is to perform a systematic investigation of a set of HgI₂ film-sample detectors under irradiation conditions relevant to mammographic, radiographic, fluoroscopic and radiotherapy imaging. X-ray sensitivities were measured and are presented in terms of an effective ionization energy (W_{EFF})—the average amount of absorbed x-ray energy required to produce each charge pair that is detected by an external means (Antonuk *et al* 2004). Other properties, such as the magnitude and temporal variation of the dark current, the electron mobility–lifetime product and the temporal behaviour of the x-ray signal response of the detectors have also been measured. To our knowledge, this study represents the first examination of the response of polycrystalline HgI₂ to radiotherapy-energy x-rays. This also represents the first systematic investigation of the signal properties of a single set of polycrystalline HgI₂ detectors across the entire range of x-ray energies corresponding to the most likely clinical application of direct detection AMFPIs incorporating HgI₂.

2. Materials and methods

2.1. HgI₂ film detectors

The HgI₂ film detectors used in this study were fabricated at Real-Time Radiography using both a physical vapour deposition (PVD) method and a particle-in-binder (PIB) method, the latter involving a screen-print process. As illustrated in figure 1, the composition of each film detector is as follows: a glass substrate coated with a layer of indium tin oxide (ITO), which serves as the bottom electrode; a barrier layer with a thickness in the range of several microns (the function of which is described below); a layer of PVD or PIB polycrystalline HgI₂ film; an isolated, top electrode in the form of a circular-shaped palladium layer ranging in area from 40 to 49 mm² from detector to detector; and a thin, polymer encapsulation to prevent evaporative degradation of the HgI₂ and to help insure long-term stability of the detector. Platinum wires connected to the top and bottom electrodes of each detector serve to allow the application of a bias voltage across the photoconductor as well as to allow measurement of current.

Specifications for the film detectors examined in this study are presented in table 1. For each detector, the identifier, type of HgI₂ film (PVD or PIB), film thickness and barrier layer code provided by the manufacturer (A, B and Dx.x) are presented. Barrier layer types A, B and D correspond to different, doped polymer materials and the variations of type D correspond to small changes in the electrical conductivity of the material—with the manufacturer providing

Table 1. Technical specifications of the polycrystalline mercuric iodide film detectors examined in this study. The density of the PVD form of the HgI₂ material is believed to be 95%–100% of that of single-crystal HgI₂, 6.36 g cm⁻³, and a value of 100% was assumed in the Monte Carlo simulations. The composition of the PIB material is 90% HgI₂ and 10% polymer, by weight, corresponding to 50% HgI₂ and 50% polymer, by volume.

Detector ID	Material type	Thickness (μm)	Barrier layer type
PVD-230	PVD	230	D2
PVD-240a	PVD	240	A
PVD-240b	PVD	240	D2.1
PVD-260	PVD	260	D1
PIB-320	PIB	320	B
PIB-458	PIB	458	D2

the codes, but not the types of polymer. In addition, the barrier layers for the PVD- and PIB-coated detectors were $\sim 1.5 \mu\text{m}$ and $3.0 \mu\text{m}$ thick, respectively. The configurations of HgI₂ and barrier layers studied correspond to those currently under examination on active matrix, flat-panel imagers (AMFPIs) (Antonuk *et al* 2004). In the case of arrays, the choice of the type and thickness of barrier layer material is critical for: (a) preventing chemical reactions between HgI₂ and certain metals in the array designs (e.g., aluminium); (b) compensating for adverse effects associated with the presence of significant (i.e., $>1 \mu\text{m}$) variations in the surface uniformity of array prior to photoconductor deposition and (c) minimizing dark current—and is a topic of on-going research. However, chemical reactions and surface non-uniformities are not issues with the film detectors and no obvious correlation between barrier type and dark current or radiation signal properties was apparent in the present studies.

2.2. Measurement techniques

For each film detector, dark and x-ray measurements were performed at electric field strengths of up to $2 \text{ V } \mu\text{m}^{-1}$ across the detector, achieved through application of a negative bias voltage to the top electrode. In particular, x-ray data were acquired under irradiation conditions (beam energies and filtration, exposures or doses, geometry) representative of those used in mammography, radiography, fluoroscopy (involving diagnostic-quality x-rays) and radiotherapy imaging (involving megavoltage x-rays). For conciseness, the corresponding measurements and results shall be referred to as mammographic, radiographic, fluoroscopic and radiotherapy, respectively. As illustrated in figure 2, detector dark current and x-ray-induced photocurrent were sampled using a picoammeter and a current preamplifier, respectively, connected to a digitizer and/or a data acquisition card in a PC.

For each electric field, x-ray photocurrent was measured at four different exposures (at diagnostic x-ray energies) or irradiation times (at megavoltage energies). Data acquisition extended from $\sim 5 \text{ s}$ before to $\sim 25, 25, 5$ and 5 s after the irradiation, for the mammographic, radiographic, fluoroscopic and radiotherapy measurements, respectively. For the measurements performed with diagnostic x-rays, exposure was determined using a dosimeter (Keithley 35050A) connected to a calibrated ion chamber (Keithley 96035B for mammographic energies; Keithley 96035 for radiographic/fluoroscopic energies). The chamber was placed in the radiation field in the vicinity of the detector during x-ray measurements. For measurements performed with megavoltage x-rays, the amount of radiation used was quantified in terms of the irradiation time, specified in monitor units (MUs). The radiation source was calibrated such that one MU delivers 0.8 cGy of dose for a field size of $10 \times 10 \text{ cm}^2$ at a depth of 10 cm in water at a distance of 100 cm from the radiation source.

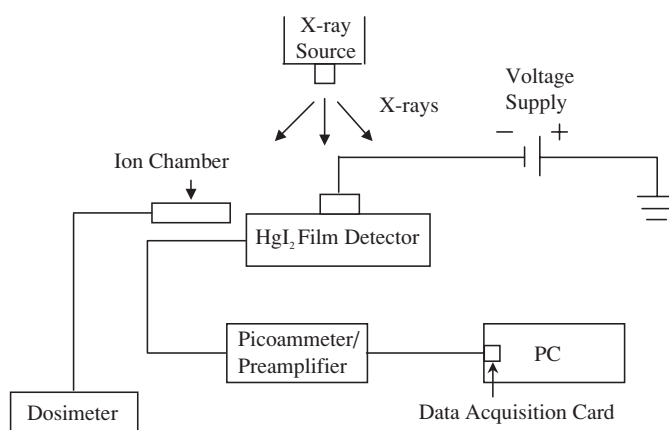


Figure 2. Block diagram representation of various elements involved in the acquisition of data from the HgI₂ film detectors. Note that a picoammeter and a preamplifier were used for dark current and x-ray-induced photocurrent measurements, respectively. Also note that, for each film detector, the entire area of the glass substrate was irradiated during measurements.

The dark current from each detector was measured at a sampling rate of 0.2 Hz using a picoammeter (Keithley 485) connected to a data acquisition card (PCI-GPIB, National Instruments). In addition, the temporal variation of dark current for each detector was measured for a period of 1 h at an electric field of $1 \text{ V } \mu\text{m}^{-1}$. For the measurements at diagnostic x-ray energies, the detector current was converted to voltage using a current preamplifier with a maximum bandwidth of 100 kHz (ORIEL 70710, ORIEL Instruments), and the output voltage signal was digitized using a digitizer card (PCI-4452, National Instruments) at a sampling rate of 1 kHz. For the radiotherapy measurements, the bandwidth of x-ray pulses from the linear accelerator (pulse width of $\sim 4 \mu\text{s}$ at a repetition rate of $\sim 60 \text{ Hz}$) exceeded the bandwidth of the current preamplifier used for the diagnostic measurements. Therefore, the photocurrent was converted to voltage using a different, high-speed, current preamplifier with a maximum bandwidth of 100 MHz (DHPCA-100, FEMTO Messtechnik GmbH), and the output voltage signal was digitized using a different digitizer card (PCI-6111, National Instruments) at a sampling rate of 1 MHz.

For the mammographic measurements, a mammographic x-ray source (Senographe DMR, GE Medical Systems) was used. Results were obtained at an x-ray energy of 26 kVp with a Mo target with an inherent filtration of $30 \mu\text{m}$ of Mo and with additional filtration in the form of a standard, tissue-equivalent, breast phantom with a 5 cm thickness (BR-12, Nuclear Associates). The radiation provided by the source is nearly constant in intensity during an exposure and turns on and off within $\sim 5 \text{ ms}$. The x-ray source-to-detector distance was 65 cm. Data were acquired with 40, 80, 125 and 160 mA s irradiations corresponding to exposures of $\sim 4, 8, 12.5$ and 16 mR, respectively.

For the radiographic and fluoroscopic measurements, a Dunlee PX1415 x-ray tube incorporating a Tungsten target with a Picker MTX380 high-frequency generator operated in radiographic and fluoroscopic mode, respectively, was used. Results were obtained at an x-ray energy of 72 kVp, with an inherent filtration of 3.2 mm Al and with an additional filtration of 20 mm Al. The x-ray source-to-detector distance was 100 cm. For the radiographic measurements, unless otherwise specified, data were acquired with 100, 200, 320 and 400 ms irradiations at a tube current of 10 mA, corresponding to exposures of $\sim 0.15, 0.31, 0.51$ and 0.65 mR, respectively. For the fluoroscopic measurements, data were acquired during

a ~ 2 min continuous irradiation at a tube current of 4 mA, corresponding to an exposure rate of ~ 0.3 mR s $^{-1}$. The radiation provided by the source is nearly constant in intensity during an exposure (the level of the intensity being determined by the tube current) and, for radiographic operation, turns on and off within ~ 10 ms.

For the radiotherapy measurements, a 6 MV beam was provided by a standard radiotherapy linear accelerator (Linac 21EX, Varian). The x-ray source-to-detector distance was 142 cm. Data were acquired with 4, 8, 12 and 16 MU irradiations, delivered at a dose rate of 100 MU min $^{-1}$. A 1 mm thick sheet of copper was positioned over the HgI $_2$ detector—corresponding to the use of such material for build-up and scatter rejection in radiotherapy imaging (Antonuk 2002). Non-conducting tape (~ 220 μ m thick) applied to the underside of the copper prevented electrical contact with the top contact of the film detector. The presence of this tape, plus a very small air gap (less than ~ 50 μ m) between the film detector and the taped copper sheet, had a negligible effect upon the signal measurements.

The geometry of the top and bottom electrodes of the film detectors, along with the fact that the entire detector was irradiated during measurements (see figures 1 and 2), allows for the possibility of signal collection outside of the detector volume directly below the area of the top electrode. Such contributions would arise from a non-uniform extension of the electric field into this volume. If present, these would artificially inflate the empirically-determined dark current and x-ray sensitivities, and thereby diminish the W_{EFF} values, reported in this paper. In addition, the Hecht relation (which is used in the analysis of the data and which assumes a uniform electric field) would not apply for the component of signal collected near and outside the boundaries of the top contact. Empirical investigations conducted independently of the studies reported below indicated the possibility of such ‘edge’ effects—with the size of the effect increasing with increasing electric field strength. However, for the range of electric field strengths used in these studies (up to 2 V μ m $^{-1}$), an upper limit for the fraction of the total signal originating from outside the region below the top contacts was only $\sim 4\%$ under mammographic conditions (where the incident radiation largely interacts in the upper part of the film detector) and $\sim 10\%$ under radiographic conditions (where the radiation interacts throughout the volume of the detector). Since the experimental uncertainties in these results are comparable to the size of the results themselves, and given the apparently modest size of these contributions, no correction for this effect was applied to the empirical data reported in this paper.

2.3. Determination of x-ray sensitivity and effective ionization energy

After digitization, the photocurrent from the detector was numerically integrated after dark current subtraction and, through an appropriate calibration, transformed into the amount of charge extracted from the detector. Generally, the magnitude of this charge was found to increase in a highly linear manner with increasing radiation. Thus, for a given set of conditions (detector, beam energy, electric field, etc), the x-ray sensitivity was determined from the slope of a plot of detector charge as a function of delivered radiation.

In order to objectively evaluate and compare the performance of the HgI $_2$ detectors across different film thicknesses, x-ray energies and electric field strengths, a simple metric was introduced. This metric, referred to as the effective ionization energy, W_{EFF} , is defined as the average amount of absorbed x-ray energy required to produce each charge pair that is detected in the measurement.

The following equation was used to calculate the effective ionization energy:

$$W_{\text{EFF}} = \frac{E_{\text{DEPOSITED}}}{N_e} \text{ (eV)}, \quad (1)$$

where $E_{\text{DEPOSITED}}$ is the total energy (in eV) absorbed in the HgI₂ per unit radiation and N_e is the total corresponding charge (in electrons) measured by the data acquisition system.

To determine $E_{\text{DEPOSITED}}$, calculations involving Monte Carlo simulations of x-ray photons interacting with HgI₂ material were performed at the energies corresponding to the measurements. The Monte Carlo simulations were performed using the EGS4 Monte Carlo code (Nelson and Rogers 1989) and the RZ_PHS user code (Jaffray *et al* 1995). For calculations performed at diagnostic x-ray energies, x-ray spectra corresponding to appropriate peak energies and beam filtrations were obtained from references (Boone *et al* 1997, Boone and Seibert 1997). For calculations performed at radiotherapy energies, an x-ray spectrum from Sheikh-Bagheri (1999) was used. In all the calculations, a geometry consisting of a parallel pencil beam irradiating the centre of a 40 cm diameter disc of HgI₂ was assumed. In these simulations, disc thicknesses corresponding to those of the actual film detectors were used, and densities corresponding to 100% and 50% of the single-crystal density of HgI₂ were assumed for the cases of PVD and PIB, respectively. In the case of the radiotherapy calculations, 1 mm of Cu was added on top of the HgI₂ layer as build-up material.

2.4. Determination of mobility–lifetime product

Two material properties of HgI₂, mobility (μ) and lifetime (τ) of the free charge carriers, are indicators of the film quality, and are strongly affected by the process of fabricating the detector material. The $\mu\tau$ product was determined by means of the Hecht relation (Hecht 1932):

$$Q = Q_0 \frac{\mu\tau E}{d} \left(1 - \exp\left(\frac{-d}{\mu\tau E}\right) \right). \quad (2)$$

For a detector of thickness d , this expression relates the amount of x-ray-induced charge collected from the detector, Q , to the total charge generated in the detector by the incident radiation, Q_0 , and the electric field applied across the detector, E . The mobility–lifetime product was determined by fitting this expression to the collected charge plotted as a function of electric field.

The Hecht relation can be used to determine the $\mu\tau$ product under conditions in which the detected charge carriers are generated near one electrode of the detector and drift across the detector under the influence of a uniform electric field. Under such conditions, the charge detected by external electronics is primarily due to the transport of charge carriers of a single polarity (electron or hole) across the film. In figure 3, x-ray attenuation is plotted as a function of HgI₂ film thickness for the various x-ray beam spectra used in the Monte Carlo simulations described above. In the case of mammographic x-rays, the majority of the photons are attenuated very close to the top electrode, compared to the attenuation profiles of radiographic/fluoroscopic and radiotherapy x-ray photons that are more evenly distributed across the detector thickness. Given that the $\mu\tau$ product for electrons is significantly higher than for holes in polycrystalline HgI₂ (Zuck *et al* 2003, Street *et al* 2002), measurements performed at mammographic x-ray energies, with a negative bias voltage applied to the top electrode of a film detector, resulted in a relatively unambiguous determination of $\mu\tau$ for electrons, using the Hecht relation.

3. Results

In this section, results are reported for film detectors operated under conditions relevant to mammographic, radiographic, fluoroscopic and radiotherapy imaging as well as in the absence

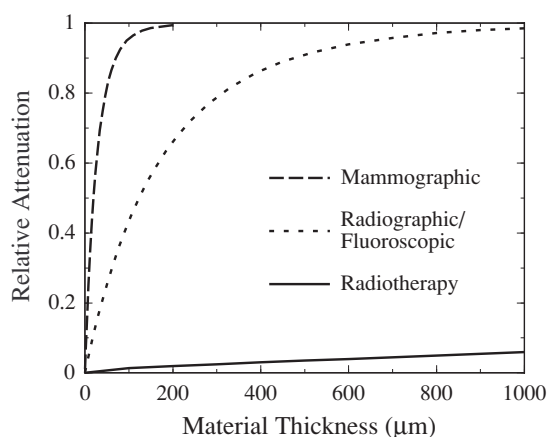


Figure 3. Relative attenuation of x-rays as a function of HgI_2 material thickness for polyenergetic x-ray spectra corresponding to mammographic (26 kVp), radiographic/fluoroscopic (72 kVp) and radiotherapy (6 MV) conditions.

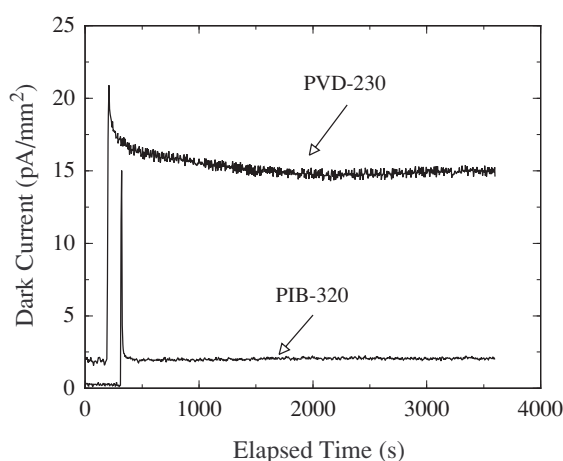


Figure 4. Dark current plotted as a function of elapsed time for representative PVD and PIB film detectors at an electric field strength of $1 \text{ V } \mu\text{m}^{-1}$. For both data sets, the dark current surges for a brief period when the electric field is first applied.

of radiation. For each set of conditions, results are shown for four or six of the detectors listed in table 1—with two of the detectors exhibiting abnormal behaviour during later studies as a result of considerable handling. In addition, illustrations of specific detector behaviour under each set of conditions are presented for a pair of ‘representative’ detectors (PVD-230 and PIB-320) whose performance was typical of that of the various PVD and PIB detectors, respectively.

3.1. Dark current measurements

Dark current data acquired at $1 \text{ V } \mu\text{m}^{-1}$ over a period of 1 h for the representative film detectors are presented in figure 4. For both detectors, the magnitude of the measured current surged to relatively high levels upon initial application of the electric field. Subsequently,

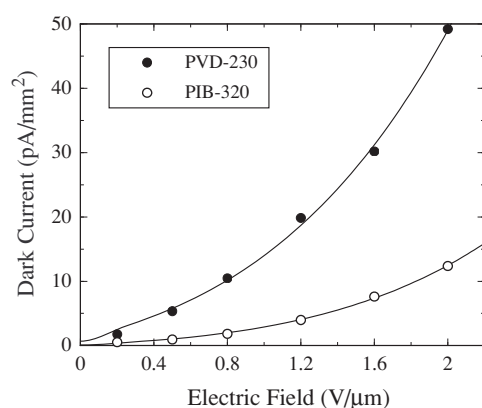


Figure 5. Dark current plotted as a function of electric field, E , for representative PVD and PIB film detectors. The curves correspond to fitting the data with a function of the form $\alpha \times e^{\beta \times \sqrt{E}}$ (Simmons 1967) where α and β were parameters in the fit.

the current settled to lower, stable levels by ~ 1600 s and ~ 60 s after the application of bias voltage to the PVD and PIB detectors, respectively. This asymptotic settling behaviour is possibly due to charge depletion from defect states within the band gap. As time increases, a condition of steady-state thermal generation is established and the dark current approaches a stable value. Similar behaviour has been observed in polycrystalline PbI₂ film detectors (Street *et al* 1999). In addition, the PIB detector exhibits a much lower dark current than that of the PVD detector—consistent with results from earlier polycrystalline HgI₂ studies (Schieber *et al* 2000). This lower dark current is believed to be due to the inhibiting effect of the non-conducting polymer component in the PIB material (Schieber *et al* 1999).

Measurements of dark current under conditions of temporal stability were performed for all film detectors at electric fields ranging from 0.2 to 2.0 V μm^{-1} and results for the two representative detectors are presented in figure 5. For all detectors, the dark current was found to increase with increasing electric field in a non-ohmic, super-linear fashion, as illustrated in the figure. In the case of single-crystal HgI₂ detectors of the same general construction, dark current is typically influenced by either the Poole–Frenkel effect or the Richardson–Schottky effect (Simmons 1967, Frenkel 1938), which lower the Coulombic potential barrier in the bulk of the photoconductor or at the interface of the electrode and photoconductor, respectively. Both effects strongly influence the conductivity of a photoconductor and lead to dark current behaviour that varies as the exponential of the square root of the electric field strength applied across the detector (Simmons 1967, Mellet and Friant 1989). A fit of the present dark current data with a function exhibiting this dependence is also shown in the figure. The good agreement between the data and the fit supports the idea that the dark current of the present polycrystalline HgI₂ film detectors is strongly influenced by the Poole–Frenkel or Richardson–Schottky effects.

For the film detectors in this study, the measured dark currents ranged from ~ 0.1 pA mm^{-2} to ~ 130 pA mm^{-2} for the specified range of electric field strengths. While increasing electric field strength across the detector generally increases the x-ray sensitivity of a photoconductive material up to some asymptotic limit, the dark current also increases with electric field, as noted above. Thus, in order to incorporate HgI₂ (or any photoconductor) into a direct detection AMFPI, the desire to maximize x-ray sensitivity must be balanced against practical considerations concerning the magnitude of the dark current. Generally, practical AMFPI

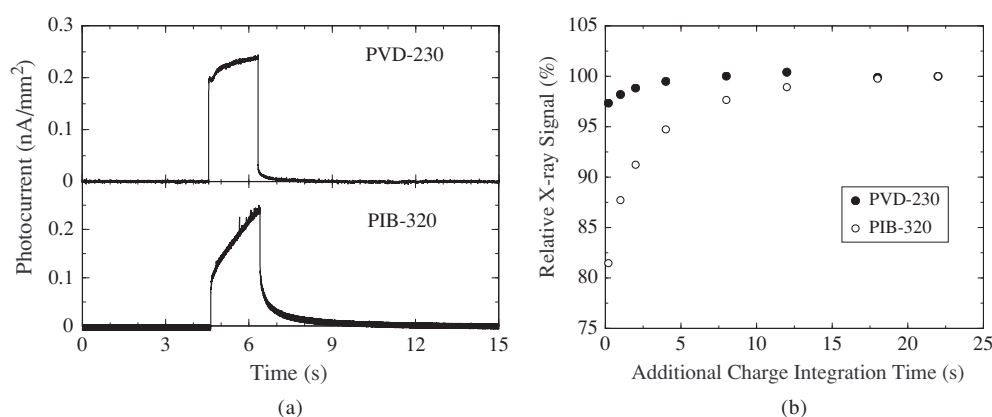


Figure 6. Results from representative PVD and PIB detectors obtained under mammographic conditions. (a) Photocurrent waveforms measured at an electric field of $2 \text{ V } \mu\text{m}^{-1}$ at an exposure of $\sim 13 \text{ mR}$. The dark current contribution, determined from the average photocurrent prior to the radiation exposure, has been subtracted. (b) X-ray signal plotted as a function of the additional time (beyond the end of the radiation exposure) used in the numerical integration of the photocurrent waveforms in (a). The signals have been normalized to the value obtained with an additional integration time of 22 s—so that the final point for each detector is, by definition, at 100%.

Table 2. The electric field value for each film detector that results in a dark current level of 10 pA mm^{-2} , E_T .

Detector ID	E_T ($\text{V } \mu\text{m}^{-1}$)
PVD-230	0.77
PVD-240a	0.73
PVD-240b	1.30
PVD-260	0.53
PIB-320	1.80
PIB-458	2.00

operation requires that the dark current not exceed a maximum on the order of 10 pA mm^{-2} (Antonuk 2004). Higher values result in relatively large (and undesirable) shot noise contributions (Maolinbay *et al* 2000) and significantly reduce the capacity of the pixels to store imaging charge. With these considerations in mind, the electric field strength resulting in a ‘tolerable’ level of dark current, 10 pA mm^{-2} was empirically determined for each HgI_2 film detector from the acquired data. Table 2 lists the value of this ‘threshold’ electric field (E_T) for each detector. For the detectors studied, the dark current limit for the PVD detectors is exceeded for fields below $1 \text{ V } \mu\text{m}^{-1}$, while the limit for the PIB detectors is not exceeded until significantly higher field strengths (on the order of $\sim 2 \text{ V } \mu\text{m}^{-1}$) are reached. Compared to an earlier study of similarly configured detectors (Gilboa *et al* 2002), the present E_T values for the four PVD detectors are higher, indicating a lower dark current behaviour.

3.2. Mammographic measurements

Mammographic data were acquired at electric fields ranging from 0.05 to $2.0 \text{ V } \mu\text{m}^{-1}$. Current waveforms of the representative PVD and PIB detectors obtained at an electric field of $2.0 \text{ V } \mu\text{m}^{-1}$ are presented in figure 6(a). The shape of these waveforms is governed by the temporal structure of the radiation pulse (described in the ‘Measurement techniques’ section)

and by the properties of signal extraction from the detectors—and is further influenced by the electric field strength. (This also generally applies to the radiographic and radiotherapy waveforms discussed below.) During irradiation, the current was observed to increase (as shown in the figure), remain the same or even decrease—depending upon the irradiation time and field strength. For each detector and exposure condition, the radiation-induced charge is obtained by integrating current waveforms such as those of figure 6(a). A comparison between the waveforms of the two detectors reveals a longer signal decay time for the PIB detector after termination of the radiation exposure—a characteristic that was observed for all PIB detectors. Long decay times are a manifestation of non-negligible charge trapping and slow charge release in the photoconductor material (Antonuk *et al* 1997). This can lead to charge loss (due to charge trapping) during acquisition of single images (e.g., mammography or radiography) or charge carry-over between consecutive frames (due to charge release) during acquisition of consecutive image frames (e.g., fluoroscopy)—referred to as image lag.

To quantify the degree of charge trapping and release, radiation-induced charge from the two film detectors was measured at a field strength of $2.0 \text{ V } \mu\text{m}^{-1}$ as a function of additional integration time beyond the end of radiation exposure. The results are presented in figure 6(b). In the figure, the integrated charge has been normalized to the charge obtained when the integration time extends to 22 s beyond the end of the exposure. For the PVD detector, the response is relatively fast, with 97% of the total charge being collected when the integration time is extended to 200 ms beyond the end of the exposure. In comparison, for the same integration time the PIB exhibits a considerably slower response with only ~82% of the total charge collected. For the various PVD detectors, charge collected for integration time extending 200 ms beyond the end of the exposure ranged from 94% to 99%, whereas for the two PIB detectors it was 82% and 86%. Note that the interval chosen for extending the integration (200 ms) is a value typical for AMFPIs operated in a single image acquisition mode. (For this reason, the same interval was used in the determination of radiographic and radiotherapy sensitivity.)

X-ray sensitivity plotted as a function of applied electric field for the representative film detectors is shown in figure 7. For both detectors, x-ray sensitivity increases with increasing electric field before reaching an asymptotic level of maximum collection efficiency. The PVD detector is seen to exhibit a faster increase in sensitivity resulting in the maximum being reached at a lower electric field. Values of the electron mobility–lifetime product ($\mu\tau$) for the detectors, obtained from fitting data such as those shown in figure 7 using equation (2), are summarized in table 3. The values of $\mu\tau$ for the PIB detectors are found to be generally lower than for the PVD detectors, in agreement with earlier studies (Street *et al* 2002). This is probably due to signal-inhibiting effects associated with the binder in the PIB material that reduces the mobility of the charge carriers.

From film detector results such as those shown in figure 7, an electric field strength, E_α , corresponding to sensitivity values equal to 90% of the asymptotic level, was determined through interpolation of the data. Values of E_α for the film detectors, shown in table 3, represent a desirable operational condition for achieving relatively large sensitivity. However, such a condition may come at the cost of high dark current, which is found to increase in a super-linear fashion with electric field, resulting in the need to balance high sensitivity against low dark current for practical AMFPI operation. As seen in table 3, E_α is at least a factor of 2 lower than E_T for the PIB detectors, indicating that these detectors exhibit efficient charge collection at electric field strengths that generate acceptably low levels of dark current. For the PVD detectors, this is not always the case, indicating that further reductions in dark current are needed in order to achieve a reasonable balance between good collection efficiency and low dark current. At an electric field of E_α , PVD detectors generally exhibit higher sensitivities,

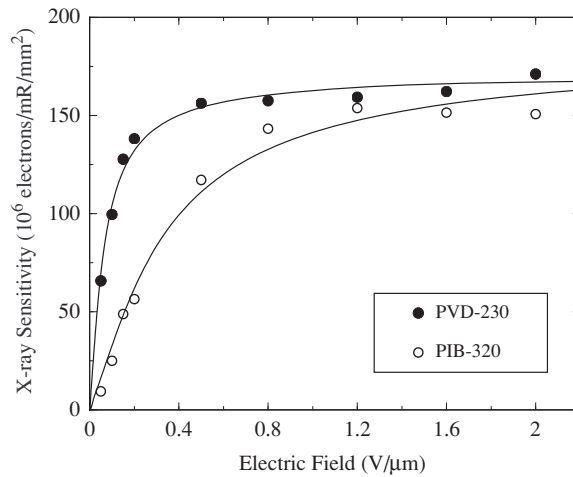


Figure 7. X-ray sensitivity of representative PVD and PIB detectors, obtained under mammographic conditions, plotted as a function of electric field. The curves correspond to fitting the data with a function of the form given by equation (2).

Table 3. Summary of results obtained under mammographic conditions for each film detector. These results include the mobility–lifetime product ($\mu\tau$), electric field strengths E_α , x-ray sensitivity and effective ionization energy (W_{EFF}) at E_α , and W_{EFF} at E_T . For purposes of comparison in this and following tables, the electric field strengths E_T (from table 2) are also listed. See the text for details.

Detector ID	$\mu\tau$ ($\text{cm}^2 \text{V}^{-1}$)	E_T ($\text{V } \mu\text{m}^{-1}$)	E_α ($\text{V } \mu\text{m}^{-1}$)	Sensitivity at E_α ($10^6 \text{ e mR}^{-1} \text{ mm}^{-2}$)	W_{EFF} at E_α (eV)	W_{EFF} at E_T (eV)
PVD-230	2.09×10^{-5}	0.77	0.46	154	5.7	5.5
PVD-240a	5.76×10^{-6}	0.73	0.89	125	7.2	7.0
PVD-240b	3.82×10^{-5}	1.30	1.02	153	5.7	5.6
PVD-260	8.75×10^{-5}	0.53	0.12	143	6.1	6.0
PIB-320	5.71×10^{-6}	1.80	0.71	136	6.4	5.7
PIB-458	1.47×10^{-5}	2.00	0.69	115	7.6	6.9

and thus lower effective ionization energy values, than PIB detectors (see table 3). Note that, for some PVD detectors, the value of W_{EFF} approaches the value corresponding to the single-crystal form of HgI_2 , $\sim 5 \text{ eV}$ (Zuck *et al* 2003, Street *et al* 2002). These W_{EFF} results are generally lower than previously reported values of 6.7 eV and 7.8 eV obtained from AMFPI prototype arrays, with PVD HgI_2 films, operated under similar irradiation conditions (Street *et al* 2002, Schieber *et al* 2001).

3.3. Radiographic and fluoroscopic measurements

For the studies under radiographic and fluoroscopic conditions, data were acquired from four film detectors at electric fields ranging from 0.05 to $2.0 \text{ V } \mu\text{m}^{-1}$. Current waveforms of the representative PVD and PIB detectors obtained at an electric field of $2.0 \text{ V } \mu\text{m}^{-1}$ under radiographic conditions are presented in figure 8(a). From these data, it can be seen that the temporal decay of the photocurrent after termination of radiation is only slightly longer for the PIB detector, which is contrary to what was observed under mammographic conditions. This

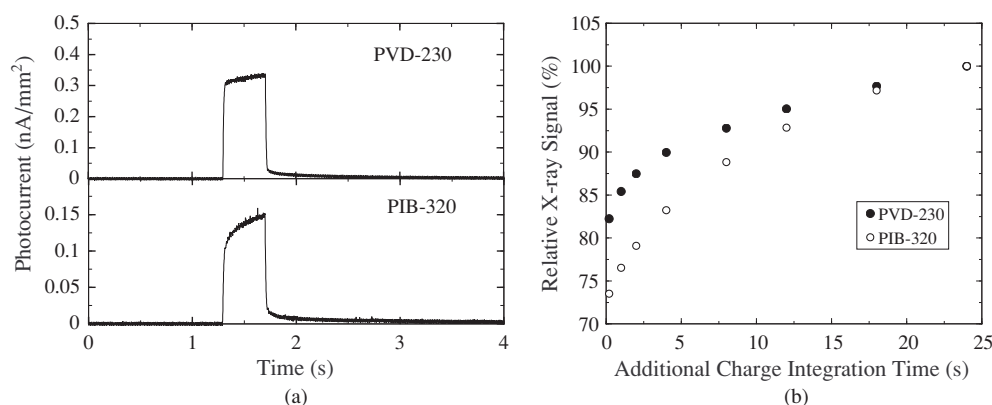


Figure 8. Results from representative PVD and PIB detectors obtained under radiographic conditions. (a) Photocurrent waveforms, after subtraction of the dark current contribution, measured at an electric field of $2 \text{ V } \mu\text{m}^{-1}$ at an exposure of $\sim 0.65 \text{ mR}$. (b) X-ray signal plotted as a function of the additional time (beyond the end of the radiation exposure) used in the numerical integration of the photocurrent waveforms in (a). The signals have been normalized to the value obtained with an additional integration time of 24 s.

change in temporal response for the PIB detector is probably a manifestation of the change in the profile of x-ray interactions across the thickness of the detector at the higher radiographic energies.

The temporal decay of photocurrent after termination of the radiation is a manifestation of charge trapping and release in the photoconductor, and can affect charge collection as seen in figure 8(b). This figure shows the integrated charge of the waveforms of figure 8(a), plotted as a function of additional integration time beyond the end of the radiation. For example, a charge integration time extending to 200 ms beyond the end of radiation results in a charge collection efficiency of 82% and 74% for PVD and PIB detectors, respectively. These values are somewhat lower than those obtained at mammographic energy, most likely due to the more uniform distribution of x-ray interactions in the photoconductor thickness resulting in significantly larger contributions of holes in the charge collection/trapping process. Finally, note that the increase of signal during the irradiation of the PVD and PIB detectors is similar to that observed under mammographic conditions in figure 6(a).

Current waveforms for the representative PVD and PIB film detectors, obtained under fluoroscopic conditions at $0.2 \text{ V } \mu\text{m}^{-1}$ and at $0.8 \text{ V } \mu\text{m}^{-1}$, are presented in figures 9(a) and (b), respectively. While the data at $0.8 \text{ V } \mu\text{m}^{-1}$ exhibit an increase in current up to a stable level, those at $0.2 \text{ V } \mu\text{m}^{-1}$ exhibit an initial surge, followed by a decrease down to a stable level. This initial variation of current at the lower electric field ($0.2 \text{ V } \mu\text{m}^{-1}$) is possibly due to polarization effects in the detector where uncollected charges effectively reduce the applied electric field. This results in the reduction of photocurrent until an equilibrium between charge trapping and release is reached leading to a stable current level. For all film detectors, such polarization effects were observed only at low electric fields, and were absent above $1 \text{ V } \mu\text{m}^{-1}$.

Figures 10(a) and (b) show x-ray sensitivities as a function of electric field for the representative PVD and PIB detectors, respectively, under radiographic and fluoroscopic conditions. While the reported radiographic sensitivity is based on the integration of photocurrent up to 200 ms beyond the end of radiation exposure, the fluoroscopic sensitivity is based on the integration of photocurrent only in the part of the waveform exhibiting a stable current level where charge trapping and release effects are in equilibrium. For both detectors,

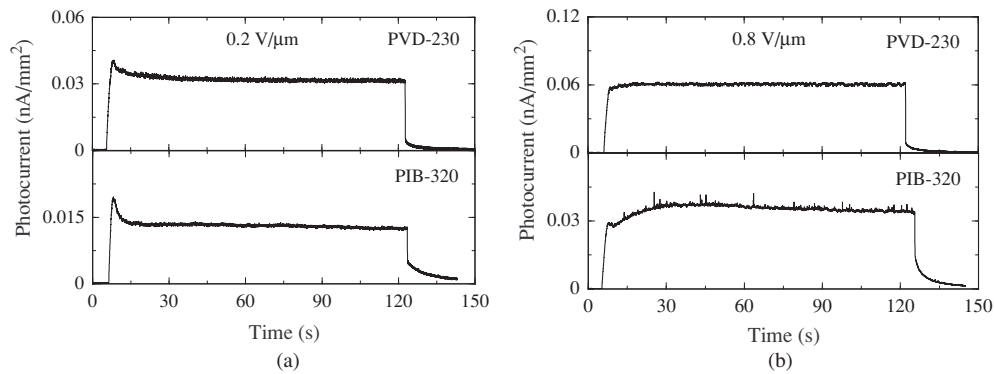


Figure 9. Photocurrent waveforms, after subtraction of the dark current contribution, for representative PVD and PIB detectors obtained under fluoroscopic conditions at electric field strengths of (a) $0.2 \text{ V } \mu\text{m}^{-1}$ and (b) $0.8 \text{ V } \mu\text{m}^{-1}$.

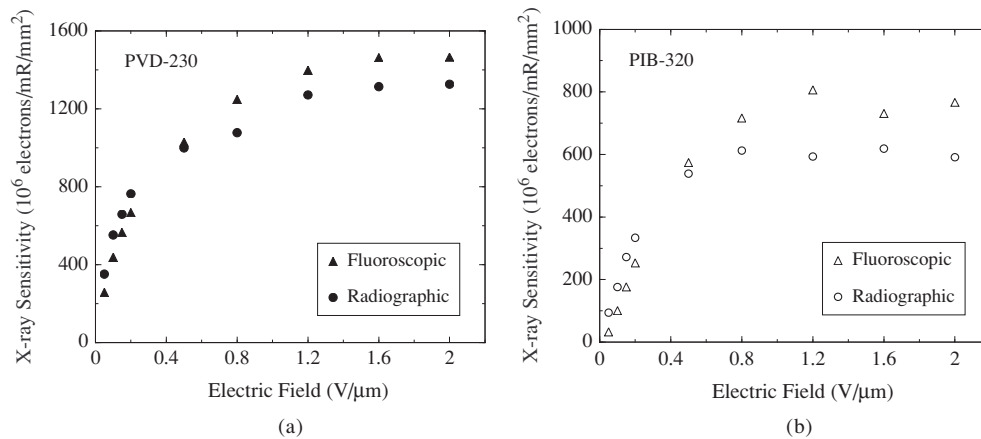


Figure 10. X-ray sensitivity of representative (a) PVD and (b) PIB detectors, obtained under radiographic and fluoroscopic conditions, plotted as a function of electric field.

x-ray sensitivity is found to increase with increasing electric field before reaching a maximum at $\sim 1 \text{ V } \mu\text{m}^{-1}$. At high electric field, both detectors exhibit a sensitivity that is higher under fluoroscopic conditions than under radiographic conditions, most likely due to the equilibrium of charge trapping and release under fluoroscopic conditions (Antonuk *et al* 1997). However, at low electric fields (i.e., $< 0.4 \text{ V } \mu\text{m}^{-1}$) the trend is reversed due to a significant reduction in fluoroscopic signal caused by the polarization effect noted in the discussion of figure 9(a) data. This behaviour has been independently observed by others (Zentai *et al* 2003) on similar film detectors.

A study was also performed on the same representative film detectors under radiographic conditions to examine the degree of constancy in the detector signal response when a fixed amount of radiation is delivered at different levels of intensity. The extent to which the signal remains constant under such circumstances is a direct measure of the degree to which the detector exhibits reciprocity in its response—with no variation being desirable (Antonuk *et al* 1994). In the study, the radiation intensity was varied by a factor of 10 through variation of the x-ray tube current. This study was performed with a fixed exposure of $\sim 2 \text{ mR}$ and at two different electric field strengths, 0.5 and $1.6 \text{ V } \mu\text{m}^{-1}$, corresponding to relatively low and

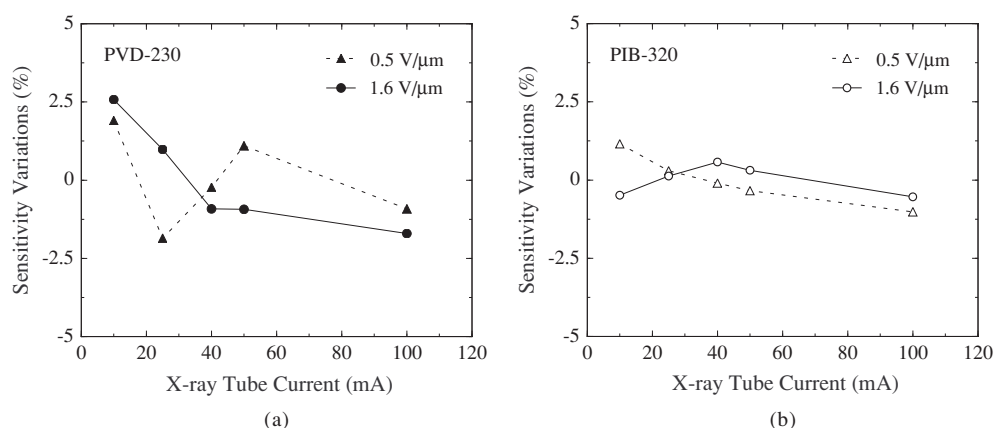


Figure 11. Variations in x-ray sensitivity of representative (a) PVD and (b) PIB detectors, plotted as a function of x-ray tube current, for two electric field strengths. These results were derived from x-ray sensitivity data, obtained at a constant exposure of ~ 2 mR, under radiographic conditions for a given detector and field strength. Each plotted point corresponds to the percentage deviation from the average sensitivity for that data set. Dashed and solid lines connect data obtained at 0.5 and 1.6 $\text{V } \mu\text{m}^{-1}$, respectively.

Table 4. Summary of results obtained under radiographic and fluoroscopic conditions for four of the film detectors. These results include electric field strengths E_α , x-ray sensitivity and effective ionization energy (W_{EFF}) at E_α , and W_{EFF} at E_T . See the text for details.

Detector ID	E_T ($\text{V } \mu\text{m}^{-1}$)	Radiation condition	E_α ($\text{V } \mu\text{m}^{-1}$)	Sensitivity at E_α ($10^6 \text{ e mR}^{-1} \text{ mm}^{-2}$)	W_{EFF} at E_α (eV)	W_{EFF} at E_T (eV)
PVD-230	0.77	Radio	1.04	1194	7.5	8.3
		Fluoro	0.99	1318	6.8	7.3
PVD-260	0.53	Radio	1.57	1102	8.6	10.7
		Fluoro	0.61	1124	8.5	8.5
PIB-320	1.8	Radio	0.47	532	13.4	11.8
		Fluoro	0.75	691	10.3	9.5
PIB-458	2.0	Radio	0.52	682	13.1	10.8
		Fluoro	0.85	993	9.0	8.4

almost complete charge collection efficiency, respectively. As illustrated in figures 11(a) and (b), the degree of reciprocity failure at both electric fields is observed to be less than $\sim 2.5\%$ and $\sim 1.2\%$ for the PVD and PIB detectors, respectively—values that are only slightly greater than the estimated experimental error of approximately $\pm 1\%$ for these measurements. This is a highly favourable result and is lower than the value of $\sim 6\%$ observed from indirect detection AMFPI arrays (Antonuk *et al* 1994).

For four of the film detectors, table 4 contains a summary of values obtained empirically under radiographic and fluoroscopic conditions. These values are electric field strength E_α (defined in a manner parallel to that used in the mammography studies), sensitivity at E_α and effective ionization energy at E_α and E_T . The PIB detectors exhibit values for E_α smaller than for E_T , as was the case under mammographic conditions, and again demonstrating the potential of PIB HgI₂ for use as a direct detection AMFPI converter in radiographic and fluoroscopic

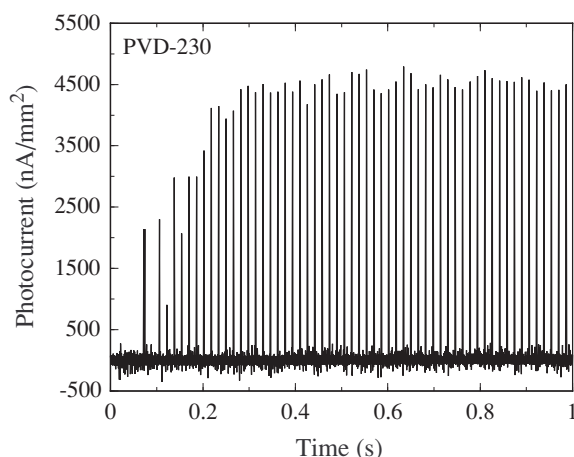


Figure 12. Photocurrent waveform, after subtraction of the dark current contribution, for a representative PVD detector obtained under radiotherapy conditions at an electric field strength of $2.0 \text{ V } \mu\text{m}^{-1}$. The peaks in the waveform correspond to the first ~ 57 pulses of an irradiation.

applications. In addition, the PVD detectors exhibit values for E_{α} greater than for E_{T} —indicating that further improvement in dark current is required for practical AMFPI operation. Compared to the results for the PIB detectors, the W_{EFF} values for the PVD detectors are lower under both radiographic and fluoroscopic conditions—consistent with trends observed in the mammographic studies. In addition, both the radiographic and fluoroscopic W_{EFF} values are greater than those obtained under mammographic conditions. This is likely due to the fact that, under radiographic conditions, the more uniform distribution of the charge generated by incident x-rays across the thickness of the detector reduces the contribution of higher mobility carriers (electrons) to the measured x-ray signal. Finally, all W_{EFF} values obtained under fluoroscopic conditions are slightly lower than those obtained under radiographic conditions—a result consistent with the fact that the radiographic measurements are affected by charge trapping whereas the fluoroscopic measurements are not (Antonuk *et al* 1997). These values of W_{EFF} are generally lower than previously reported values of $\sim 10 \text{ eV}$ and $\sim 25 \text{ eV}$ obtained from PVD and PIB HgI_2 films on AMFPI prototype arrays, respectively, under comparable irradiation conditions (Street *et al* 2002, Schieber *et al* 2001).

3.4. Radiotherapy measurements

Figure 12 shows a typical current waveform obtained from a PVD film detector under radiotherapy conditions. The larger peaks correspond to the response of a detector to $\sim 4 \mu\text{s}$ radiation pulses delivered by the linear accelerator, one pulse every $\sim 16 \text{ ms}$. The uneven increase in the height of these peaks in the first $\sim 0.3 \text{ s}$ of radiation is largely due to changes in the radiation output from the accelerator when the beam is first turned on. The smaller spikes (i.e., those with signals less than 500 nA mm^{-2}) appearing between these peaks are due to noise pickup. A more detailed view of the response of representative PVD and PIB detectors to an individual pulse is shown in figure 13. Both detectors exhibit a fast response when subjected to such short-duration radiation pulses and the corresponding decay times between beam pulses (on the order of $10 \mu\text{s}$) are relatively brief compared to decay times observed under mammographic and radiographic conditions (on the order of 100 ms). Furthermore,

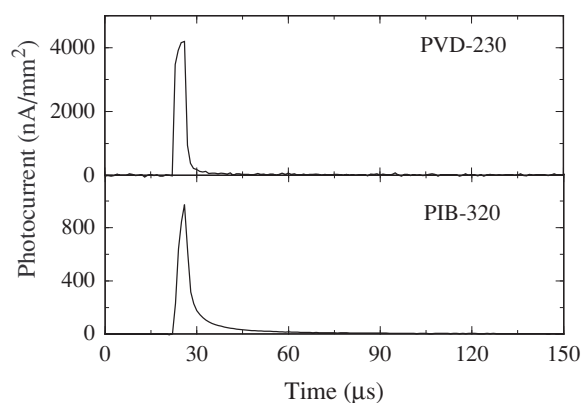


Figure 13. Photocurrent waveforms of a single radiation pulse for representative PVD and PIB detectors obtained under radiotherapy conditions. In each case, the dark current contribution, determined from the average photocurrent prior to the pulse, has been subtracted.

both PVD detectors exhibit a faster signal decay time than the PIB detectors, as was previously noted for the mammographic and radiographic data.

In order to determine the x-ray-induced signal, and thus x-ray sensitivity, it is necessary to integrate photocurrent waveforms such as those shown in figure 12. Due to limitations in the stability of the electronic offset of the preamplifier output, the response to individual radiation pulses were integrated separately. Each integration was performed from the leading edge of the response to a given pulse, to just before the next pulse, subtracting a baseline obtained from detector dark current in the ~ 1 ms interval immediately preceding the integration period. (For a given waveform, the integration of the response to the final pulse extends to 200 ms beyond that pulse.) The results obtained from all of the pulses are then summed in order to determine the total signal for the waveform. In this manner, systematic baseline trends persisting longer than the ~ 16 ms interval between pulses were largely removed from the integration process. While such an analysis technique may fail to completely account for signal contributions from release of charge for time scales longer than 16 ms, these contributions are believed to be rather small, as suggested by the waveforms of figure 13.

Figure 14 shows x-ray sensitivities as a function of electric field strength for four of the film detectors. For each detector, sensitivity increases with increasing electric field but does not exhibit the same degree of convergence towards an asymptotic limit by $\sim 2 \text{ V } \mu\text{m}^{-1}$ as was observed under mammographic and radiographic conditions. This behaviour suggests reduced charge collection efficiency, likely due to the more uniform x-ray interaction and energy deposition across the detector thickness at megavoltage energies, resulting in a relatively larger contribution of the lower mobility charge carriers (holes) to the collected signal. Since the sensitivities of the detectors do not reach a maximum over the range of field strengths examined, an electric field strength, E_α , (and an effective ionization energy at E_α) cannot be precisely determined for purposes of comparison with results obtained at diagnostic energies, as previously discussed. In their place, values of W_{EFF} at the highest field studied, $2 \text{ V } \mu\text{m}^{-1}$, are listed in table 5. These values are found to be generally higher than the W_{EFF} values at E_α obtained under mammographic, radiographic and fluoroscopic conditions (see tables 3 and 4)—another indication of reduced charge collection efficiency under radiotherapy conditions. In addition, it is interesting to note that, while the PVD and PIB detectors have similar x-ray detection efficiencies (as listed in table 5), the PIB detectors

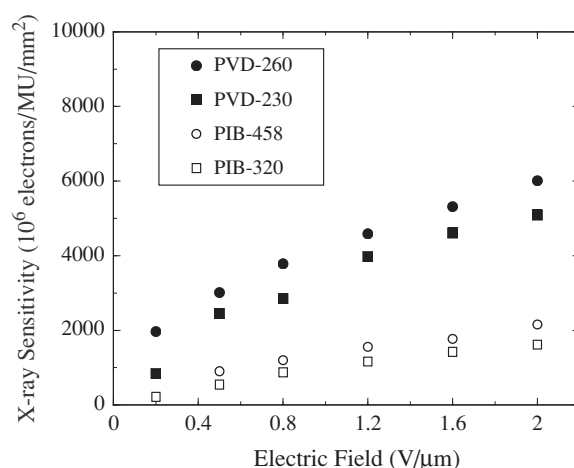


Figure 14. X-ray sensitivity of four of the film detectors, obtained under radiotherapy conditions, plotted as a function of electric field.

Table 5. Summary of results obtained under radiotherapy conditions for four of the film detectors. These results include x-ray detection efficiencies, x-ray sensitivity and effective ionization energy (W_{EFF}) at $2 \text{ V } \mu\text{m}^{-1}$, and W_{EFF} at E_{T} . See the text for details.

Detector ID	Detection efficiency (%)	E_{T} ($\text{V } \mu\text{m}^{-1}$)	Sensitivity at $2 \text{ V } \mu\text{m}^{-1}$ ($10^6 \text{ e MU}^{-1} \text{ mm}^{-2}$)	W_{EFF} at $2 \text{ V } \mu\text{m}^{-1}$ (eV)	W_{EFF} at E_{T} (eV)
PVD-230	2.08	0.77	5094	7.4	13.4
PVD-260	2.25	0.53	6012	7.5	14.5
PIB-320	1.70	1.8	1620	15.2	16.1
PIB-458	2.08	2.0	2161	17.4	17.4

exhibit values of W_{EFF} at $2 \text{ V } \mu\text{m}^{-1}$ over two times higher than for the PVD detectors. This is consistent with results from the mammographic, radiographic and fluoroscopic studies and provides further support for the idea that non-conducting nature of the binder material in PIB impedes charge collection. A further consequence of the reduced charge collection efficiency under radiotherapy conditions is that values of W_{EFF} at an electric field strength of E_{T} (given in table 5) are generally higher than those observed under mammographic, radiographic and fluoroscopic conditions (see tables 3 and 4).

4. Discussion and conclusions

In this investigation, the dark current and radiation signal properties of a photoconductive material, mercuric iodide, have been examined under irradiation conditions relevant to mammographic, radiographic, fluoroscopic and radiotherapy x-ray imaging. These studies were performed on a set of film detectors having a relatively simple construction containing a layer of polycrystalline HgI_2 (created either by physical vapour deposition (PVD) or by a screen-print process resulting in a particle-in-binder (PIB) composite) and a barrier layer, sandwiched between a pair of opposing electrode plates. The measurements were performed with electric field strengths across the photoconductor ranging from 0.05 to $2.0 \text{ V } \mu\text{m}^{-1}$. These studies were undertaken as part of a larger programme of research to investigate the use of this photoconductive material as the x-ray converter component in direct detection,

active matrix, flat-panel imagers. In particular, results obtained from the present studies provide unambiguous information about the x-ray detection properties of the two forms of polycrystalline HgI₂, compared to signal information obtained from HgI₂-coated AMFPI arrays which is affected both by the design of the array and by the manner in which such arrays are operated. Data obtained from film detectors therefore serve a valuable role in the interpretation of array data and in predicting limits to imager performance.

The dark current results obtained from the film detectors are encouraging, but also indicate the need for further improvement. The PIB detectors exhibited significantly lower dark current than the PVD detectors, most likely due to the inhibiting effect of the non-conducting polymer component of the PIB material. Furthermore, under biasing conditions that allow extraction of a very large fraction (~90%–100%) of the x-ray-generated signal, the PIB detectors exhibited dark currents below 10 pA mm⁻²—an upper limit for practical AMFPI operation—while the PVD detectors generally did not. However, given that commercially-available AMFPIs exhibit dark current levels of ~1 pA mm⁻², or lower, further reduction in this parameter is necessary for both PVD and PIB HgI₂ in order to maximize the range of exposures over which an array will operate without pixel saturation. The precise level of dark current required for optimal operation will, of course, depend upon the details of the design and operation of the imager and the modality (e.g., mammography, radiography, fluoroscopy or radiotherapy). Furthermore, the radiotherapy application would benefit from substantially thicker detectors in order to stop a larger fraction of the megavoltage beam. However, the component of dark current arising from bulk effects in the HgI₂ material can reasonably be expected to increase with thickness. Therefore, for the radiotherapy application, the challenge of achieving sufficiently low dark current with a thick detector presently favours the PIB form of the material, which has exhibited significantly lower dark current in these early studies.

The results of the x-ray studies lead to a variety of interesting and important conclusions. The polycrystalline HgI₂ photoconductors exhibit a temporal response that results in the release of a non-negligible amount of signal charge following an irradiation at diagnostic energies. This delayed release amounts to up to ~25% additional charge under mammographic conditions and up to ~30% under radiographic conditions. By comparison, for commercially-available AMFPIs, the quantity of signal charge that is measured in the first frame following readout of a mammographic or radiographic irradiation (called first field lag) is only on the order of ~5%–10% (Antonuk 2004). Therefore, the use of HgI₂ in direct detection AMFPIs under fluoroscopic conditions could give rise to motion blur and/or ghosting artefacts during acquisition of consecutive image frames. For other applications such as mammography, radiography and radiotherapy, which are based on the acquisition of single images, the signal loss resulting from the trapping that leads to the delayed release of charge should not be a problem, given the high sensitivity of the material, however, the potential for ghosting (Siewerdsen and Jaffray 1999) exists. Thus, some reduction in charge trapping and release in polycrystalline HgI₂ would be generally desirable.

The measurements also indicate that, under all irradiation conditions examined (mammographic, radiographic, fluoroscopic and radiotherapy), the polycrystalline HgI₂ photoconductive material provides higher x-ray sensitivities (and lower effective ionization energies, W_{EFF}) than the x-ray converter materials used in present commercially-available AMFPIs (a-Se, Gd₂O₂S:Tb and needle-structured CsI:Tl). (Examples of W_{EFF} values for these detector materials are shown in table 6.) Furthermore, at both diagnostic and radiotherapy energies, the PVD form of the material exhibited lower values of W_{EFF} than the PIB form. Moreover, the most favourable (i.e., lowest) values of W_{EFF} for both PVD and PIB were observed under mammographic conditions—with the PVD results approaching the W_{EFF} of the single-crystal form of HgI₂ (~5 eV). In addition, results obtained under mammographic,

Table 6. Effective ionization energy values for x-ray converter materials of the type commonly used in active matrix, flat-panel imagers. The values given for Gd₂O₂S:Tb and CsI:Tl were obtained using equation (1) with the denominator empirically determined under fluoroscopic conditions using AMFPI prototypes (corrected for the optical collection fill factor and the coupling efficiency of the pixel photodiodes (Antonuk *et al* 2000)) and the numerator calculated using Monte Carlo simulations (as for the HgI₂ film detectors). The scintillators used in these determinations were a Lanex Regular (Gd₂O₂S:Tb) screen and a needle-structure CsI:Tl screen (with an overlying white reflective layer), with surface densities of ~ 70 and 203 mg cm^{-2} , respectively. The value for a-Se was obtained from reference (Rieppo and Rowlands 1997). For purposes of comparison, the W_{EFF} value for the single-crystal form of HgI₂ is also given (Zuck *et al* 2003, Street *et al* 2002).

Converter material	W_{EFF} (eV)
Gd ₂ O ₂ S:Tb	~ 25
CsI:Tl	~ 24
a-Se	~ 50
HgI ₂ (single crystal)	~ 5

radiographic and fluoroscopic conditions indicate that the application of an electric field in the range of $1\text{--}2 \text{ V } \mu\text{m}^{-1}$ is sufficient for maximizing charge collection efficiencies. Such field strengths are considerably lower than the $\sim 10 \text{ V } \mu\text{m}^{-1}$ required for a-Se photoconductors (Zhao and Rowlands 1995). Overall, polycrystalline HgI₂ is a definite candidate for improving the signal-to-noise performance of AMFPIs under conditions of low exposure or high spatial frequencies, such as are encountered in fluoroscopic and mammographic imaging, respectively.

While some forms of x-ray imaging would benefit from the significantly greater sensitivity offered by HgI₂, the higher x-ray energies associated with radiotherapy imaging generate sufficiently large signals that only modest detector sensitivity, and thus higher W_{EFF} , is desirable and necessary to avoid pixel saturation. For radiotherapy imaging, the important issue is the need for improved x-ray detection efficiency (Sawant *et al* 2005). Even for the modest thicknesses employed in the film detectors of this study, the corresponding detection efficiencies are equivalent to those of the phosphor screens used in commercial AMFPIs (El-Mohri *et al* 2001). While thicker layers of polycrystalline HgI₂ (that would lead to corresponding improvements in detection efficiency) are technically feasible (Schieber *et al* 2000), such detectors must be developed with careful consideration given to achieving low dark current and an appropriate level of sensitivity.

Acknowledgments

The authors wish to extend their appreciation to Mr Douglas Berry for valuable and enthusiastic assistance with the measurements and data analysis. This work was supported by National Institutes of Health grants R01-EB000558, R01-CA76405 and R01-CA51397.

References

- Antonuk L E 2002 Electronic portal imaging devices: a review and historical perspective of contemporary technologies and research *Phys. Med. Biol.* **47** R31–65
- Antonuk L E 2004 a-Si:H TFT-based active matrix flat-panel imagers for medical x-ray applications *Thin Film Transistors, Materials and Processes vol 1: Amorphous Silicon Thin Film Transistors* vol 1, ed Y Kuo (Boston: Kluwer) pp 395–484
- Antonuk L E, El-Mohri Y, Siewerdsen J H, Yorkston J, Huang W, Scarpine V E and Street R A 1997 Empirical investigation of the signal performance of a high-resolution, indirect detection, active matrix flat-panel imager (AMFPI) for fluoroscopic and radiographic operation *Med. Phys.* **24** 51–70

- Antonuk L E, Jee K-W, El-Mohri Y, Maolinbay M, Nassif S, Rong X, Zhao Q, Siewerdsen J H, Street R A and Shah K S 2000 Strategies to improve the signal and noise performance of active matrix, flat-panel imagers for diagnostic x-ray applications *Med. Phys.* **27** 289–306
- Antonuk L E, Siewerdsen J H, Yorkston J and Huang W 1994 Radiation response of amorphous silicon imaging arrays at diagnostic energies *IEEE Trans. Nucl. Sci.* **41** 1500–5
- Antonuk L E, Zhao Q, Su Z, Yamamoto J, El-Mohri Y, Li Y, Wang Y and Sawant A R 2004 Systematic development of input-quantum-limited fluoroscopic imagers based on active matrix, flat-panel technology *Proc. SPIE* **5368** 127–38
- Boone J M, Fewell T R and Jennings R J 1997 Molybdenum, rhodium, and tungsten anode spectral models using interpolating polynomials with application to mammography *Med. Phys.* **24** 1863–74
- Boone J M and Seibert J A 1997 An accurate method for computer-generating tungsten anode x-ray spectra from 30 to 140 kV *Med. Phys.* **24** 1661–70
- Capp M P 1981 Radiological imaging—2000 A.D. *Radiology* **138** 541–50
- Colbeth R E *et al* 2001 40 × 30 cm² Flat-panel imager for angiography, R&F, and cone-beam CT applications *Proc. SPIE* **4320** 94–102
- El-Mohri Y, Antonuk L E, Jee K-W, Kang Y, Li Y, Sawant A, Su Z, Wang Y, Yamamoto J and Zhao Q 2003 Evaluation of novel direct and indirect detection active matrix, flat-panel imagers (AMFPIs) for mammography *Proc. SPIE* **5030** 168–80
- El-Mohri Y, Jee K W, Antonuk L E, Maolinbay M and Zhao Q 2001 Determination of the detective quantum efficiency of a prototype, megavoltage indirect detection, active matrix flat-panel imager *Med. Phys.* **28** 2538–50
- Frenkel J 1938 On pre-breakdown phenomena in insulators and electronic semi-conductors *Phys. Rev.* **54** 647–8
- Gilboa H *et al* 2002 Medical imaging with mercuric iodide direct digital radiography flat-panel x-ray detectors *Proc. SPIE* **4784** 315–25
- Granfors P R, Albagli D, Tkaczyk E J, Aufrichtig R, Netel H, Brunst G, Boudry J and Luo D 2001 Performance of a flat panel cardiac detector *Proc. SPIE* **4320** 77–86
- Hecht H K 1932 Zum Mechanismus des Lichtelektrischen Primastromers in Isolierenden Kristallen *Z. Phys.* **77** 235–43
- Ikeda S, Suzuki K, Ishikawa K, Colbeth R E, Webb C, Tanaka S and Okusako K 2003 Development and evaluation of a digital radiography system using a large-area flat panel detector *Proc. SPIE* **5030** 215–25
- Iwanczyk J S, Patt B E, Tull C R, MacDonald L R, Skinner N, Hoffman E J, Fornaro L, Mussio L, Saucedo E and Gancharov A 2001 Mercuric iodide polycrystalline films *Proc. SPIE* **4508** 28–40
- Jaffray D A, Battista J J, Fenster A and Munro P 1995 Monte-Carlo studies of x-ray-energy absorption and quantum-noise in megavoltage transmission radiography *Med. Phys.* **22** 1077–88
- Kang Y, Antonuk L E, El-Mohri Y, Hu L, Li Y, Sawant A, Su Z, Wang Y, Yamamoto J and Zhao Q 2005 Examination of HgI₂ and PbI₂ photoconductive materials for direct detection, active matrix, flat-panel imagers for diagnostic x-ray imaging *IEEE Trans. Nucl. Sci.* **52** 38–45
- Kruse J J, Herman M G, Hagness C R, Davis B J, Garces Y I, Haddock M G, Olivier K R, Stafford S L and Pisansky T M 2002 Electronic and film portal images: a comparison of landmark visibility and review accuracy *Int. J. Radiat. Oncol. Biol. Phys.* **54** 584–91
- Maolinbay M, El-Mohri Y, Antonuk L E, Jee K W, Nassif S, Rong X and Zhao Q 2000 Additive noise properties of active matrix flat-panel imagers *Med. Phys.* **27** 1841–54
- Mellet J and Friant A 1989 $I(t)$, $I(V)$ and surface effect studies of vapor grown and solution grown HgI₂ detectors *Nucl. Instrum. Methods Phys. Res. A* **283** 199–207
- Mosleh-Shirazi M A, Swindell W and Evans P M 1998 Optimization of the scintillation detector in a combined 3D megavoltage CT scanner and portal imager *Med. Phys.* **25** 1880–90
- Nelson W R and Rogers D W O 1989 Structure and operation of the EGS4 code system *Monte Carlo Transport of Electrons and Photons Below 50 MeV* ed T M Jenkins, W R Nelson, A Rindi, A E Nahum and D W O Rogers (New York: Plenum) pp 287–306
- Pang G and Rowlands J A 2004 Development of high quantum efficiency, flat panel, thick detectors for megavoltage x-ray imaging: a novel direct-conversion design and its feasibility *Med. Phys.* **31** 3004–16
- Rieppo P K and Rowlands J A 1997 X-ray imaging with amorphous selenium: theoretical feasibility of the liquid crystal light valve for radiography *Med. Phys.* **24** 1279–91
- Samei E and Flynn M J 2003 An experimental comparison of detector performance for direct and indirect digital radiography systems *Med. Phys.* **30** 608–22
- Sawant A *et al* 2005 Segmented phosphors—MEMS-based high quantum efficiency detectors for megavoltage x-ray imaging *Med. Phys.* **32** 553–65
- Sawant A, Zeman H, Samant S, Lovhoiden G, Weinberg B and DiBianca F 2002 Theoretical analysis and experimental evaluation of a CsI(Tl) based electronic portal imaging system *Med. Phys.* **29** 1042–53

- Schieber M *et al* 2000 Mercuric iodide thick films for radiological x-ray detectors *Proc. SPIE* **4142** 197–204
- Schieber M *et al* 2001 Nondestructive imaging with mercuric iodide thick film x-ray detectors *Proc. SPIE* **4335** 43–51
- Schieber M, Zuck A, Melekov L, Shatunovsky R, Hermon H and Turchetta R 1999 High flux x-ray response of composite mercuric iodide detectors *Proc. SPIE* **3768** 296–309
- Seppi E J *et al* 2003 Megavoltage cone-beam computed tomography using a high-efficiency image receptor *Int. J. Radiat. Oncol. Biol. Phys.* **55** 793–803
- Sheikh-Bagheri D 1999 Monte Carlo study of photon beams from medical linear accelerators: optimization, benchmark and spectra *Physics* (Ottawa: Carleton University)
- Siewerdsen J H and Jaffray D A 1999 A ghost story: spatio-temporal response characteristics of an indirect-detection flat-panel imager *Med. Phys.* **26** 1624–41
- Simmons J G 1967 Poole–Frenkel effect and Schottky effect in metal–insulator–metal systems *Phys. Rev.* **155** 657–60
- Street R A (ed) 2000 *Technology and Applications of Amorphous Silicon* vol 37 (Berlin: Springer)
- Street R A, Ready S E, Lemmi F, Shah K S, Bennett P and Dmitriyev Y 1999 Electronic transport in polycrystalline PbI₂ films *J. Appl. Phys.* **86** 2660–67
- Street R A, Ready S E, Van Schuylenbergh K, Ho J, Boyce J B, Nylen P, Shah K, Melekhov L and Hermon H 2002 Comparison of PbI₂ and HgI₂ for direct detection active matrix x-ray image sensors *J. Appl. Phys.* **91** 3345–55
- Tousignant O, Demers Y, Laperriere L, Nishiki M, Nagai S, Tomisaki T, Takahashi A and Aoki K 2003 Clinical performances of a 14'' × 14'' real time amorphous selenium flat panel detector *Proc. SPIE* **5030** 71–6
- Vedantham S *et al* 2000 Full breast digital mammography with an amorphous silicon-based flat panel detector: physical characteristics of a clinical prototype *Med. Phys.* **27** 558–67
- Wovk B, Shalev S and Radcliffe T 1993 Grooved phosphor screens for on-line portal imaging *Med. Phys.* **20** 1641–51
- Zentai G *et al* 2003 Mercuric iodide and lead iodide x-ray detectors for radiographic and fluoroscopic medical imaging *Proc. SPIE* **5030** 77–91
- Zentai G, Partain L, Pavylyuchova R, Proano C, Breen B, Taieb A, Dagan M, Schieber M and Gilboa H 2004 Mercuric iodide medical imagers for low exposure radiography and fluoroscopy *Proc. SPIE* **5368** 200–10
- Zhao W, Hunt D C, Tanioka K and Rowlands J A 2004 Indirect flat-panel detector with avalanche gain *Proc. SPIE* **5368** 150–61
- Zhao W and Rowlands J A 1995 X-ray imaging using amorphous selenium: feasibility of a flat panel self-scanned detector for digital radiology *Med. Phys.* **22** 1595–604
- Zhao B and Zhao W 2003 Characterization of a direct, full-field flat-panel digital mammography detector *Proc. SPIE* **5030** 157–67
- Zuck A, Schieber M, Khakhan O and Burshtein Z 2003 Near single-crystal electrical properties of polycrystalline HgI₂ produced by physical vapor deposition *IEEE Trans. Nucl. Sci.* **50** 991–7